Analyst

PAPER

View Article Online
View Journal | View Issue

Cite this: *Analyst*, 2017, **142**, 316

# Electron spin resonance and fluorescence imaging assisted electrochemical approach for accurate and comprehensive monitoring of cellular hydrogen peroxide dynamics†

Qi Xin,‡[a] Qian Liu,‡[a,b] Hameed Shah[a,b] and Jian Ru Gong*[a]

Received 8th September 2016,
Accepted 26th November 2016

DOI: 10.1039/c6an02006b

www.rsc.org/analyst

Dynamic alteration in the levels of cellular hydrogen peroxide ($H_2O_2$) is closely related to a variety of human diseases, as well as signal transduction pathways that regulate cell survival and death. Although qualitative or quantitative methods are available for measuring either intra- or extra-cellular $H_2O_2$ levels, accurate and comprehensive *in situ* detection of the real-time $H_2O_2$ dynamics of living cells remains a significant challenge. To solve this problem, a novel multi-dimensional *in situ* cell assay platform combining electrochemistry, electron spin resonance (ESR) and optical imaging is designed. In this platform, the real-time concentration of extracellular $H_2O_2$ released from stimulated cells can be accurately detected by ESR assisted chronoamperometry, while the level of intracellular $H_2O_2$ is simultaneously monitored *via* the incorporated fluorescence imaging. Accurately and simultaneously analyzing the level variations of extra- and intra-cellular reactive oxygen species based on our assay platform can complement each other for further precise and in-depth investigation of their membrane transport and related cellular signaling, which will benefit disease diagnosis and treatment.

## Introduction

Reactive oxygen species (ROS), such as hydrogen peroxide ($H_2O_2$), superoxide anion, and hydroxyl radical, are mainly produced from the intracellular mitochondrial electron transport chain and function as important mediators in a variety of biological events.[1] As a non-radical, uncharged oxidant, $H_2O_2$ is chemically more stable than other ROS and can penetrate through the cell membrane to accumulate extracellularly in the surrounding tissues.[2] Under endogenous or exogenous stimuli, the intra-/extra-cellular $H_2O_2$ concentration is ever-changing due to its continuous generation and degradation, resulting in different physiological and pathological consequences.[3] Excessive $H_2O_2$ can result in oxidative damage which is related to aging[4,5] and many deadly human diseases such as cancer,[6] neurodegenerative disorders,[7] and inflammation.[8] On the other hand, emerging evidence suggests that $H_2O_2$, at low concentrations, can act as a secondary messenger in cellular signal transduction, playing crucial roles in mitogen-activated protein kinase and nuclear factor-kappa B pathways that affect cell proliferation and death.[9–11] Therefore, it is of great significance to accurately and comprehensively detect *in situ* the cellular $H_2O_2$ dynamics for fully understanding its physiological roles and reliably diagnosing pathological symptoms.[12]

Current methods for qualitative or quantitative detection of cellular $H_2O_2$ levels mainly include electron spin resonance (ESR),[13,14] fluorescence imaging,[15,16] electrochemistry,[17–21] and chemiluminescence.[22,23] Each method has its own characteristics, advantages, as well as inherent shortcomings. ESR spectroscopy, a sensitive technique for detecting free radicals, can also be applied to quantitative analysis of $H_2O_2$,[18] by which $H_2O_2$ is first converted to a hydroxyl radical upon ultraviolet (UV) irradiation and then captured by using a spin trap agent 5,5-dimethyl-1-pyrroline *N*-oxide (DMPO) to form a stable nitroxide radical and generate the corresponding ESR signal directly related to the concentration of $H_2O_2$, providing application in accurate quantitative determination of $H_2O_2$.[14] Nevertheless, ESR is not suitable for *in situ* and real-time detection of cellular $H_2O_2$ of living cells. Fluorescence imaging

[a]*CAS Center for Excellence in Nanoscience, CAS Key Laboratory for Nanosystem and Hierarchical Fabrication, National Center for Nanoscience and Technology, Beijing 100190, P. R. China*
[b]*University of Chinese Academy of Science, Beijing 100049, P. R. China.*
*E-mail: gongjr@nanoctr.cn*

†Electronic supplementary information (ESI) available: Preparation of F–C-GO and AuNPs; contact angle, chemical composition, and morphology characterization; optimization of the concentration of F–C-GO for modification; the selectivity of the electrode towards other biologically relevant ROS and redox compounds; study of cell adhesion and proliferation on different modified electrodes; analysis of the morphological change of Hela cells after being captured by the working electrode; references. See DOI: 10.1039/c6an02006b

‡These authors contributed equally to this work.

is usually used for detecting intracellular $H_2O_2$ dynamics using a chemo-selective probe; while it lacks the ability to monitor the released extracellular $H_2O_2$ levels.[15] Among these techniques, the electrochemical method, especially the one based on the enzyme and nanomaterial co-modified electrode,[20,21] is distinguished for its good sensitivity, rapid response, and superior biocompatibility, enabling it to quantitatively analyse the dynamics of extracellular $H_2O_2$. At a certain potential, the redox current generated by electrochemical reduction or oxidation of $H_2O_2$ is directly related to its concentration.[24] However, there is an accuracy issue in this single-dimensional electrochemical detection system involving living cells because the currently available calibration curve, which reflects the quantitative relationship between the current intensity and the $H_2O_2$ concentration of the standard solutions, is made on the working electrode either before or after living cells are anchored[17,25] and is unreliable due to the following limitations in each of the cases. In the first case, the electrical conductivity and the electrochemically active surface area of the working electrode would change after the anchorage of living cells in the actual analytical system[26,27] and thus causes an inconsistency between the test conditions of calibration and actual detection, resulting in the inaccuracy in the measured concentrations of $H_2O_2$. In the second case, the added standard $H_2O_2$ solution would partly diffuse into the cells grown on the electrode and subsequently be metabolized by intracellular peroxidases and catalases,[26] making the obtained $H_2O_2$ concentrations higher than the actual one. Therefore, a more reliable calibration curve should be established to accurately reflect the quantitative relationship between the current intensity and the $H_2O_2$ concentration for monitoring the level of extracellular $H_2O_2$ released from living cells. Meanwhile, effort should also be made to achieve simultaneous monitoring of the concentration of the intra- and extra-cellular $H_2O_2$ for comprehensively analysing the spatial dynamics of $H_2O_2$.[28]

Herein, we report a multi-dimensional analytical system (Scheme 1) combining electrochemistry, ESR spectroscopy, and fluorescence imaging for accurately and comprehensively measuring the temporal and spatial $H_2O_2$ dynamics of living cells. ESR spectroscopy, which is independent of the electrode and thus avoids the aforementioned drawbacks of the single-dimensional electrochemical method, was coupled with electrochemistry to establish a more reliable calibration curve for accurate detection of extracellular $H_2O_2$. Meanwhile, fluorescence imaging for visualization of intracellular $H_2O_2$ is performed on the transparent modified working electrode in the electrochemical cell for more comprehensive monitoring of the dynamic variation of cellular $H_2O_2$.

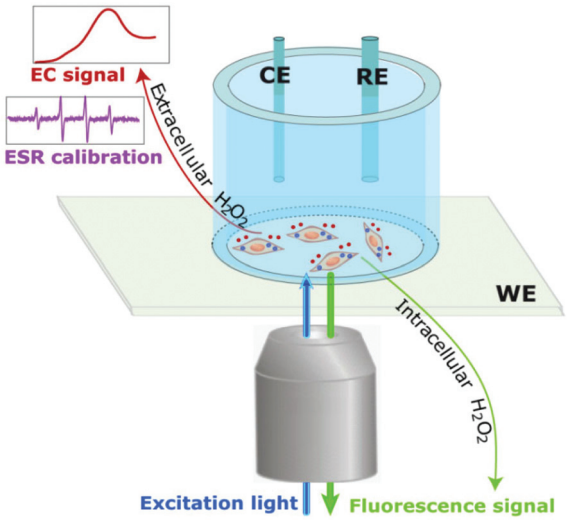


**Scheme 1** Schematic of the setup of the multi-dimensional *in situ* cell assay platform in which ESR assists the electrochemical (EC) method for accurate detection of the levels of extracellular $H_2O_2$ and the incorporated fluorescence imaging is performed on the transparent working electrode to simultaneously visualize the intracellular $H_2O_2$ variation. In the three-electrode system, a modified indium tin oxide (ITO) glass with cultured living cells was used as the working electrode (WE) with a platinum wire electrode as the counter electrode (CE) and a Ag/AgCl electrode (saturated KCl) as the reference electrode (RE).

# Experimental

## Materials and reagents

Graphite powder, horseradish peroxidase (HRP), $HAuCl_4{\cdot}H_2O$, phorbol 12-myristate-13-acetate (PMA), L-phenylalanine, and L-cysteine were purchased from Sigma-Aldrich, Inc. (USA) and used without further purification. A cyclic peptide sequence: arginine-glycine-aspartic acid-phenylalanine-cysteine (RGDFC) was purchased from Beijing Scilight Biotechnology, LCC (China). 30% $H_2O_2$ solution was purchased from Shanghai Lingfeng Chemical Reagent Co., Ltd (China), and a fresh solution of $H_2O_2$ was prepared daily. 1-Ethyl-3-(3-dimethylaminopropyl)carbodiimide hydrochloride (EDC) and *N*-hydroxysuccinimide (NHS) were purchased from Fluka Chemical Corp. (USA). Sylgard 184 silicone elastomer and curing agent were obtained from Dow Corning Corp. (USA). 5,5-Dimethyl *N*-oxide pyrroline (DMPO) was purchased from Radical Vision Inc (France). ITO-coated (150 nm thickness and resistance of 10 Ω per square) glass was purchased from HIVAC Technology Co., Ltd (China). All other chemicals were of analytical grade and used as received. The 0.1 M phosphate buffer solutions (PBS) were prepared with 0.1 M $KH_2PO_4$, 0.1 M $Na_2HPO_4$, 0.1 M $H_3PO_4$, and 0.1 M NaOH. All aqueous solutions were prepared using ultrapure water (Milli-Q 18.2 MΩ $cm^{-1}$, Millipore system).

## Characterization

The contact angle measurements were performed using a DSA 100 system. The Fourier transform infrared spectra (FTIR) of the samples were recorded between 500 and 2000 $cm^{-1}$ on an IRAffinity-1 FTIR spectrometer. Raman spectroscopy was performed using a Renishaw inVia Raman microscope with an excitation line of 514 nm provided by an argon laser. Transmission electron microscopy (TEM) images were

obtained on a Tecnai G2 20 S-TWIN electron microscope (FEI Co.), using a 200 kV accelerating voltage. X-ray photoelectron spectroscopy (XPS) data were obtained by using an ESCALab220i-XL electron spectrometer from VG Scientific using 300 W Al Kα radiation. The base pressure was about $3 \times 10^{-9}$ mbar. The binding energies were referenced to the C 1s line at 284.8 eV from adventitious carbon. ESR measurements were performed using a JEOL JES-FA 200 ESR spectrometer at X-band frequencies ($\nu \approx 9.4$ GHz). The phase-contrast and fluorescence images of Hela cells were obtained on a Nikon Eclipse Ti-S inverted fluorescence microscope.

### Electrochemical experiments

Electrochemical experiments such as cyclic voltammetry, differential pulse voltammograms, and chronoamperometry were carried out on a CHI-660b electrochemical workstation (Chenhua Instrument Company of Shanghai, China) with a conventional three-electrode system at room temperature. The working electrode was the modified ITO prepared by a layer-by-layer method. An Ag/AgCl electrode (saturated KCl) and a platinum wire worked as the reference electrode and the counter electrode, respectively. KCl (0.1 M) and $Fe(CN)_6^{3-/4-}$ were used as the supporting electrolyte solution and a redox couple, respectively, for cyclic voltammetry. PBS (0.1 M) was used as the supporting electrolyte solution for DPV and chronoamperometry. Chronoamperometry was carried out with an applied potential of −0.35 V.

### Preparation of the working electrode

The working electrode was prepared by using the transparent ITO glass as a substrate with consecutive modification of the phenylalanine (F) and cysteine (C) functionalized graphene (F–C-graphene), gold nanoparticles (AuNPs), HRP, and RGDFC cyclic peptide on the ITO surface. First, the ITO glass was cleaned by ultrasonication sequentially in acetone, alcohol, and ultrapure water for 20 min, and treated with oxygen plasma to enhance the hydrophilic property by providing a good spreading effect for further modification. Second, 10 μL of the F–C-GO aqueous solution was initially cast on the oxygen-plasma treated ITO substrate and then exposed to hydrazine vapor at 60 °C for 10 h for *in situ* reduction of F–C-GO to form a high-quality homogeneous F–C-graphene layer. Next, 10 μL of AuNP (with an average size of about 10 nm in diameter) solution was dropped onto the F–C-graphene/ITO electrode and dried at room temperature to obtain the AuNP/F–C-graphene/ITO. The detailed method for preparation of F–C-GO and AuNPs can be found in the ESI.† The prepared AuNP/F–C-graphene/ITO was sterilized with UV light irradiation for 30 min. In the following step, a homemade template (a round bottle cap) was applied for poly(dimethylsiloxane) (PDMS) cylinder fabrication. A 10 : 1 (v : v) mixture of PDMS-Sylgard Silicone Elastomer 184 and Sylgard Curing Agent 184 (Dow Corning Corp.) was poured into the cap. Then a pipe with a flat bottom (the diameter of the pipe is smaller than the cap) was inserted into the mixture and the template with the mixture was put under vacuum to remove the bubbles and cured at 70 °C for about 3 h or until the polymer was rigid. After cooling to room temperature, PDMS was carefully peeled from the master. And a hollow PDMS cylinder was obtained and fixed on the prepared AuNP/F–C-graphene/ITO using silicone gel. To decorate HRP on the electrode, AuNP/F–C-graphene/ITO was incubated in a 2 mg $mL^{-1}$ HRP solution at 4 °C for at least 24 h, followed by carefully rinsing with 0.1 M pH 7.4 PBS to remove the unadsorbed HRP. Then, 10 μL of 2 mg $mL^{-1}$ RGDFC cyclic peptide was dropped on the electrode and dried at 4 °C to avoid denaturation of the protein and the peptide. After that, Hela cells were inoculated on the modified ITO electrode *via* specific binding between the integrin receptor on cells and the RGD sequences contained in RGDFC to act as the WE.

### ESR measurement

Oxidation of the spin trap 5,5-dimethyl *N*-oxide pyrroline (DMPO), to form 5,5-dimethyl-1-pyrrolidone-*N*-oxyl (DMPOX), was monitored by ESR spectrometry to determine the extracellular $H_2O_2$ released from Hela cells. All reactions were performed in 0.1 M phosphate buffer (pH 7.4) containing 50 mM DMPO at ambient temperature. First, we used UV light to irradiate $H_2O_2$ to produce a hydroxyl radical which could be trapped by DMPO to form DMPOX, a stable nitroxide radical. And the amount of the produced $H_2O_2$ was detected as an ESR signal of the nitroxide radicals. Thus, the ESR spectra of a series of standard $H_2O_2$ solutions with known concentrations were measured to create the calibration curve. Meanwhile, the ESR signal of the solution from the electrochemical analytical system at different time points upon PMA stimulation was measured to detect the extracellular $H_2O_2$ released from living cells.

### Cell culture

The Hela cells obtained from the human epithelial carcinoma cell line, acting as a cancer cell model for the production of cellular $H_2O_2$ under stimulation, were cultured in RPMI 1640 medium (Gibco, Grand Island, NY) supplemented with 10% fetal bovine serum (FBS, Gibco, Grand Island, NY), penicillin (100 μg $mL^{-1}$), and streptomycin (100 μg $mL^{-1}$) in an incubator (5% $CO_2$, 37 °C). The cell number was determined using a Petroff–Hausser cell counter. The Hela cells for fluorescence detection were washed with buffer solution and incubated with a cell-permeable specific $H_2O_2$ probe BES–$H_2O_2$–AC (30 μM) for 30 min at 37 °C. After incubation, the stained cells were rinsed three times with buffer.

## Results and discussion

### Preparation and characterization of the working electrode

As the most critical component of electrochemical detection, a biointerface of the working electrode possessing high sensitivity, good selectivity, and strong cell adhesion was fabricated by combining F–C-graphene, AuNPs, HRP, and the RGDFC cyclic peptide *via* a layer-by-layer method[21] (Fig. 1, see detailed

 

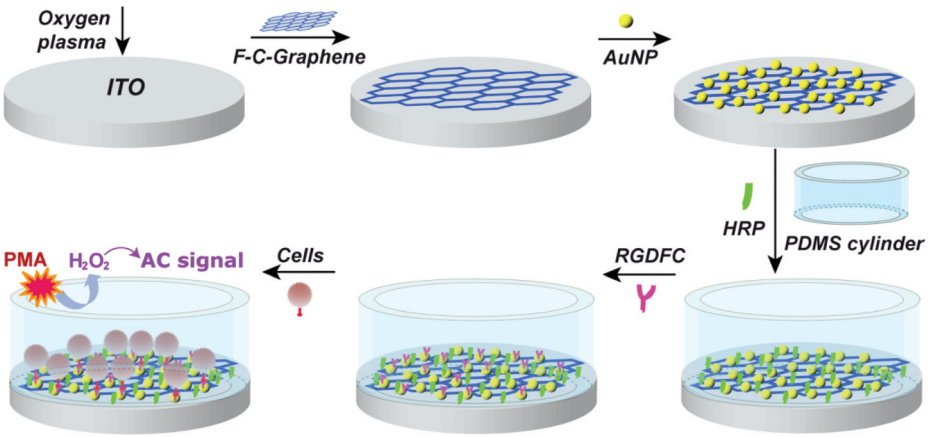


**Fig. 1** Schematic of the preparation procedure of the Hela/RGDFC/HRP/AuNP/F–C-graphene/ITO layered film. A PDMS cylinder was positioned on the ITO glass to form an electrochemical cell.

procedures in the Experimental section and Fig. S1†). The amino acid decorated F–C-graphene layer on the transparent ITO substrate not only possesses excellent electrical conductivity but also is a suitable platform for cell growth.[21,29–31] AuNPs further enhance the electrical conductivity and thus promotes detection sensitivity because the small-sized AuNPs can act as a conducting wire or an electron-conducting tunnel.[21] HRP was selected as a model enzyme since it can catalyze the electrochemical reduction of $H_2O_2$ on the electrode to generate larger electrical current compared to that of the bare ITO.[32,33] The RGDFC cyclic peptide can enhance the attachment of the living cells on the electrode *via* specific binding between the integrin receptor on cells and the RGD sequences contained in the RGDFC peptide[34,35] and facilitate the subsequent *in situ* measurement of cellular $H_2O_2$.

The amount of the modified graphene was tuned to obtain an optimal electrochemical performance of the working electrode. The cyclic voltammograms of the ITO modified with different concentrations of F–C-GO (0–1 mg $mL^{-1}$) showed that the redox peaks of the $Fe(CN)_6^{3-/4-}$ couple increased gradually with the increasing concentration of F–C-GO in the range of 0–0.06 mg $mL^{-1}$, and it began to decrease when the concentration of F–C-GO was higher than 0.06 mg $mL^{-1}$ (Fig. 2a). This is because the effect of F–C-GO on the electrochemical performance of the electrode is related to its thickness. When the F–C-GO layer is relatively thin, *i.e.* the concentration of F–C-GO is less than 0.06 mg $mL^{-1}$, the GO in the thin F–C-GO layer could be sufficiently reduced by hydrazine vapor, leading to the formation of graphene. Owing to its good conductivity and superior electrocatalytic activity, this graphene-contained layer can not only enhance the transport of electrons but also increase the effective active surface of the working electrode, eventually increasing the redox peaks of the $Fe(CN)_6^{3-/4-}$ couple in this case.[36,37] But when the number of the F–C-GO layers is further increased, *i.e.* the concentration of F–C-GO exceeds 0.06 mg $mL^{-1}$, only the GO from the upper surface of the F–C-GO layers can be reduced, leaving the electrocatalytic active surface and the F–C-GO layers under the surface unchanged. And, due to the low conductivity of the GO-contained inner layers, the transport of electrons will be certainly hindered, finally causing the decrease of the redox peak of the $Fe(CN)_6^{3-/4-}$ couple.[38] The electrode modified with F–C-GO at a concentration of 0.06 mg $mL^{-1}$ achieved the highest redox peaks, indicating its high sensitivity for electrochemical detection, and thus was used for the preparation of our working electrode (Fig. S2, ESI†). Further decoration of AuNPs onto the F–C-graphene/ITO electrode dramatically elevated the peak current (Fig. 2b) due to the effective electron transfer of AuNPs.[39] Meanwhile, the decoration of AuNPs facilitated the modification of HRP through the formation of the Au–S bond. As shown in Fig. 2c, a pair of well-defined redox peaks at −0.20 and −0.35 V in PBS (pH 7.4), which corresponded to the redox reactions of HRP,[32] was observed for HRP/AuNP/F–C-graphene/ITO, indicating that HRP retained high catalytic activity after immobilization. Differential pulse voltammograms (DPV) with high sensitivity and low background noise was applied to investigate the $H_2O_2$ detection of the modified electrode. Upon addition of $H_2O_2$, the HRP/AuNP/F–C-graphene/ITO electrode exhibited an increased peak cathodic current at −0.35 V (Fig. 2d), which was a typical representation of the catalytic reduction of $H_2O_2$, indicating that the immobilized HRP preserved a good electrocatalytic response to the reduction of $H_2O_2$. Furthermore, we investigated the selectivity of the working electrode towards $H_2O_2$ over some common coexisting ROS and redox compounds in biological systems such as hydroxyl radical, peroxynitrite, hypochlorous acid, ascorbic acid, glutamic acid, glutathione, and cysteine. The response current of RGDFC/HRP/AuNP/F–C-graphene/ITO greatly changed after the addition of $H_2O_2$ with an applied potential of −0.35 V, while nearly no current change could be observed by the addition of other biologically relevant ROS and redox compounds (Fig. S3, ESI†). This suggests that the working electrode in our work has a high selectivity toward $H_2O_2$, which could be ascribed to the $H_2O_2$-specific catalysis of HRP used in

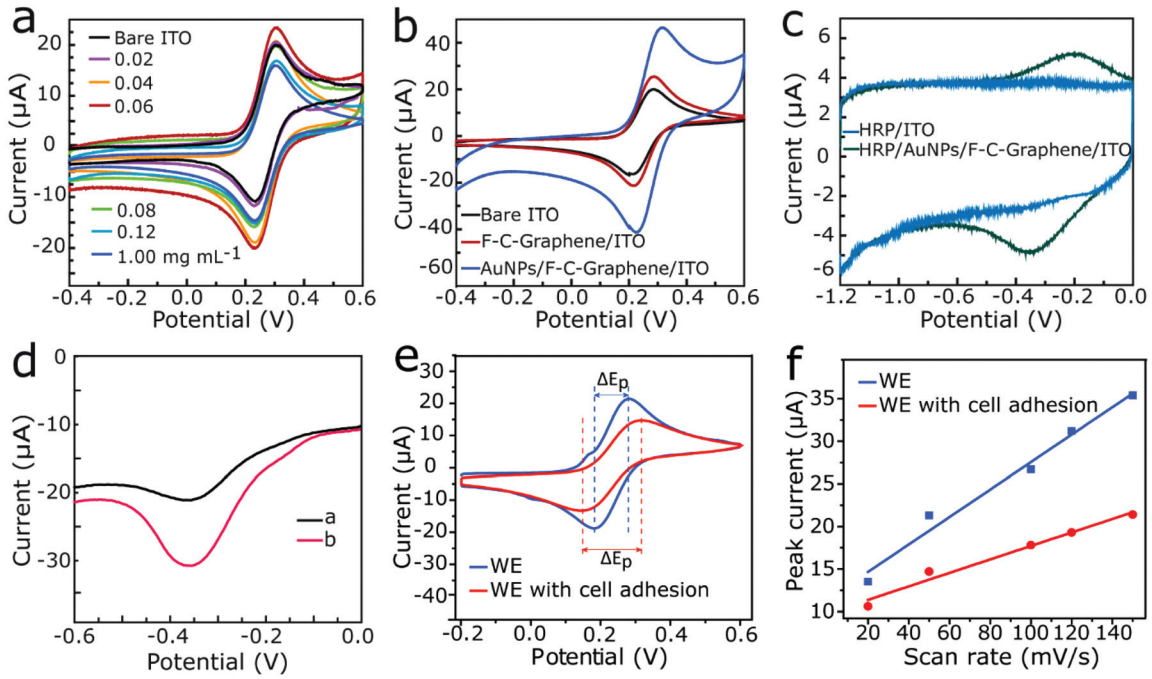


**Fig. 2** (a) Cyclic voltammograms of the modified electrode with different concentrations of F–C-graphene. (b) Cyclic voltammograms of bare ITO, F–C-graphene/ITO, and AuNP/F–C-graphene/ITO. Cyclic voltammograms in (a) and (b) were carried out in a solution of 1 mM $Fe(CN)_6^{3-/4-}$ and 0.1 M KCl at 200 mV $s^{-1}$. (c) Cyclic voltammograms of HRP/ITO and HRP/AuNP/F–C-graphene/ITO in a solution of 0.1 M PBS solution (pH = 7.4) at 100 mV $s^{-1}$. (d) DPV of HRP/AuNP/F–C-graphene/ITO from 0.0 to −0.6 V in 0.1 M PBS solution (pH 7.4) without (a) and with (b) 0.5 mM $H_2O_2$ addition. (e) Cyclic voltammograms of the working electrode with (Hela/RGDFC/HRP/AuNP/F–C-graphene/ITO) and without (RGDFC/HRP/AuNP/F–C-graphene/ITO) cell adhesion in a solution of 1 mM $Fe(CN)_6^{3-/4-}$ and 0.1 M KCl at 50 mV $s^{-1}$. (f) Plots of the peak current against the square root of scan rate ($\upsilon^{1/2}$) for the working electrode with and without cell adhesion.

our electrochemical system.[40] It is noteworthy that the data presented in Fig. 2 is the representative of the entire data set. The repeatability and reproducibility of the working electrode were evaluated by three repetitive measurements on three independent working electrodes prepared by the same layer-by-layer method. The variation coefficients (relative standard deviation) were about 5% for these assays, which showed good repeatability and reproducibility of the working electrode. Thus, the obtained HRP/AuNP/F–C-graphene/ITO electrode could offer a suitable interface with good catalytic activity and selectivity towards $H_2O_2$ production and electron transfer promoting ability.

For *in situ* monitoring of cellular $H_2O_2$, a biocompatible interface is required for good cell adhesion to facilitate cell growth and regulation of cellular functions.[41] The transparent property of the modified electrode allows the direct imaging of the grown cells by an optical microscope. It was observed that Hela cells could adhere and proliferate normally from 0 to even 72 h on RGDFC/HRP/AuNP/F–C-graphene/ITO (Fig. S4, ESI†), suggesting that this interface can capture Hela cells and efficiently retain the viability of immobilized cells owing to its good biocompatibility. Two additional experiments including scanning electron microscopy (SEM) and fluorescence staining studies, which can respectively analyze the cell surface morphology and the cell and nuclear shape, were also carried out. The SEM images of Hela cells showed that the captured cells were flat or elongated, and had numerous filopodia-like structures (Fig. S5a and S5b, ESI†), which was consistent with the normal surface morphology of Hela cells as reported by Francisco Lazaro–Dieguez.[42] Hela cells were stained with rhodamine–phalloidin for F-actin (red) and DAPI for the nucleus (blue) and analyzed with confocal laser scanning microscopy. No obvious morphological change was observed for the Hela cells on the working electrode as compared with the Hela cells in the culture dish (Fig. S5c, ESI†). The results demonstrate that the electrochemical cell has little effect on the morphology of Hela cells. Collectively, our obtained RGDFC/HRP/AuNP/F–C-graphene interface not only possesses a good electrochemical performance but also displays an excellent biocompatibility for cell adhesion, proliferation, and morphology, which is essential for electrochemical monitoring of $H_2O_2$ released from living cells.

As we discussed in the introduction part, cell adhesion could change the electrical conductivity and electrochemically active surface area of the working electrode and cause an inaccurate relationship between the current intensity and the $H_2O_2$ concentration in the single-dimensional electrochemical detection system involving living cells. Here, the influence of cell adhesion on the electrical conductivity and electrochemically active surface area of the working electrode was evaluated and demonstrated by cyclic voltammetry using $Fe(CN)_6^{3-/4-}$, which is sensitive to the surface electrochemistry of electrodes, as the redox probe. The peak potential difference ($\Delta E_p$ = 170 mV) for the working electrode with cell adhesion (Hela/RGDFC/HRP/

 

AuNP/F–C-graphene/ITO) is much larger than that ($\Delta E_p$ = 98 mV) for the working electrode without cell adhesion (RGDFC/HRP/AuNP/F–C-graphene/ITO) (Fig. 2e). The larger $\Delta E_p$ suggests the decreased electron transfer kinetics,[43] which could be ascribed to the lower electrical conductivity after anchorage of Hela cells on the working electrode.

To evaluate the changing degree of the electrochemically active surface area, the peak current $i_p$ of the cyclic voltammetry curve was compared with that for the working electrode with and without cell adhesion because the peak current $i_p$ has a quantitative relationship with the electrochemically active surface area in a diffusion-controlled electrochemical redox reaction according to the Randles–Sevcik equation:[21,44]

$$i_p = (2.99 \times 10^5)\alpha^{1/2} n^{3/2} A C D^{1/2} \upsilon^{1/2}$$

where $\alpha$, $n$, $A$, $C$, $D$ and $\upsilon$ are the charge transfer coefficient, number of electrons involved in the reaction, electrochemically active surface area, concentration of the reactant in the bulk solution (mol $cm^{-3}$), diffusion coefficient of the reactant species in solution ($cm^2$ $s^{-1}$), and scan rate of the potential perturbation (V $s^{-1}$), respectively. As the cyclic voltammogram tests for the working electrode with and without cell adhesion were both conducted using the $Fe(CN)_6^{3-/4-}$ redox couple with a concentration of 1 mM in the electrolyte of 0.1 M KCl, the parameters $\alpha$, $n$, $D$, and $C$ are the same for the two electrodes. Therefore, the peak current $i_p$ is mainly affected by the electrochemically active surface area $A$ at the same scan rate. At a scan rate of 50 mV $s^{-1}$, the redox current of $Fe(CN)_6^{3-/4-}$ for the working electrode with cell adhesion (anodic peak current: 14.7 μA) is obviously lower than that for the working electrode without cell adhesion (anodic peak current: 21.3 μA) (Fig. 2e). We further quantitatively evaluated the extent of cell adhesion influence on the electrochemically active surface area of the working electrode by plotting the peak current against the square root of scan rate. The slope of the peak current *versus* the square root of scan rate for the working electrode without cell adhesion is about 2 times larger than that for the working electrode with cell adhesion (Fig. 2f), indicating that anchorage of Hela cells can decrease the true electrochemically active surface area of the working electrode by about 50%. Collectively, both the electrical conductivity and the electrochemically active surface area of the working electrode decrease after cell adhesion. Therefore, it is necessary to introduce another technique to assist the electrochemistry for accurate quantitative analysis as the amperometric current/concentration curve established before cell adhesion is unreliable for measuring the dynamics of the extracellular $H_2O_2$ diffused from the anchored cells.

### Accurate quantitative detection of extracellular $H_2O_2$ of living cells

The quantitative evaluation of the dynamics of extracellular $H_2O_2$ released from living cells grown on the well-designed RGDFC/HRP/AuNP/F–C-graphene/ITO interface was explored by the chronoamperometric response (an electrochemical detection technique measuring the current–time curve) with the assistance of ESR. In the electrochemical analysis, the Hela cell line was employed as a model of human cells, and phorbol 12-myristate-13-acetate (PMA)—a diacylglycerol analogue activating protein kinase C to trigger $H_2O_2$ production in human cells—was used as the stimulus.[45] As shown in Fig. 3a, a continuously increased cathodic current was observed for Hela cells grown on the electrode under PMA stimulation (cyan curve) for 60 min, while no meaningful response was observed for the electrode without cultured cells under PMA stimulus (pink curve) or that with cultured cells in the absence of PMA stimulus (black curve), indicating that the observed cathodic current was ascribed to the PMA-induced $H_2O_2$ released from cultured cells and the increase in current intensity was directly related to the continuous release of $H_2O_2$ from living cells.

To achieve the reliable quantitative evaluation of the extracellular $H_2O_2$ with high accuracy, ESR spectroscopy was introduced to establish the calibration curve of ESR signal intensity *versus* $H_2O_2$ concentration as well as the relation curve of ESR signal intensity *versus* current intensity. In another duplicated electrochemical cell inoculated with the same number of Hela cells for electrochemical tests, a small amount (10 μL) of solution was taken out after the cultured cells were stimulated with PMA for different time periods and transferred to a capillary for ESR measurement. It should be noted that 10 μL of PBS solution containing the same concentration of PMA was added into the electrochemical cell to keep the total volume unchanged during ESR analysis. As shown in Fig. 3b, the obtained ESR spectra displayed four peaks with a signal intensity ratio of 1 : 2 : 2 : 1 and the hyperfine coupling constants ($a_H$ = $a_N$ = 1.49 mT) corresponding well to the previously reported values of DMPO–OH, indicating that the signal results from trapped $^{\bullet}OH$.[46] It was calculated that the ESR signal intensity reached the highest value at around 40 min and then remained stable. Thus, we chose the current–time curve in the range of 20 to 40 min as a linear analysis range for quantitative detection of extracellular $H_2O_2$ levels, which might be a main process of continuous $H_2O_2$ generation and diffusion by the cells.[47] And we found that the ESR signal intensity ($\Delta I_{ESR}$) at 20, 25, 30, 35, and 40 min showed a linear relationship with the cathodic current ($\Delta i_p$) at the same time points (inset of Fig. 3d):

$$\Delta I_{ESR} = 60.3 + 731.5\Delta i_p \quad \text{(I)}$$

where the correlation coefficient is 0.995 ($n$ = 5). In addition, we measured the ESR spectra of a series of standard $H_2O_2$ solutions with known concentrations. The ESR signal intensity increased with the increasing concentration of $H_2O_2$ standard solution (Fig. 3c). A calibration curve of the ESR signal intensity as a function of the logarithmic value of $H_2O_2$ concentrations in the range of $1 \times 10^{-6}$–$5 \times 10^{-5}$ M was plotted in Fig. 3d. And a linear regression equation of this calibration curve was obtained as follows:

$$\Delta I_{ESR} = 1995.3 + 273.0\log C_{H_2O_2} \quad \text{(II)}$$

where the correlation coefficient is 0.997 ($n$ = 5).

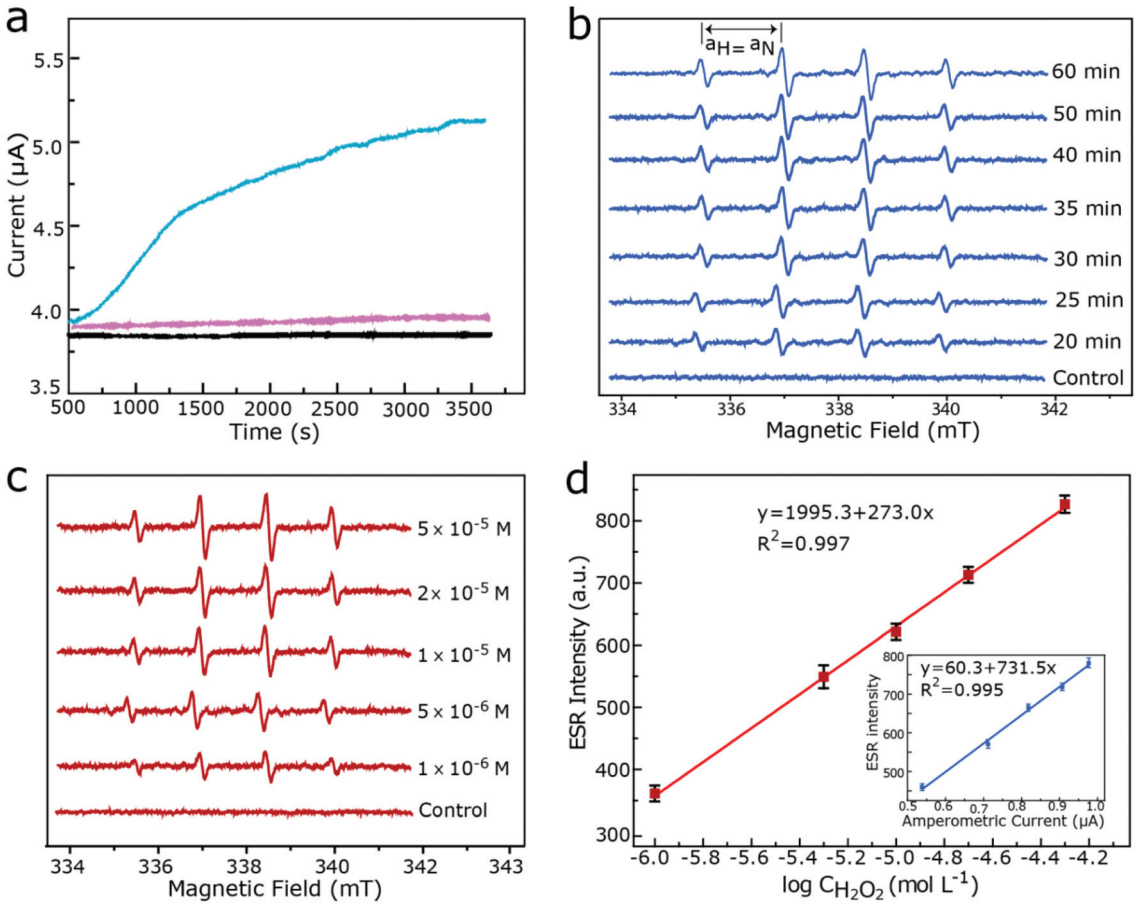


**Fig. 3** (a) The cyan curve is the chronoamperometric response of Hela cells ($5 \times 10^5$ cells per mL) on RGDFC/HRP/AuNP/F–C-graphene/ITO under PMA (10 μg mL$^{-1}$) stimulation at −0.35 V in 0.1 M PBS (pH = 7.4). The pink and black curves are the control experiments of the electrodes without cultured cells under PMA stimulus and with cultured cells in the absence of PMA stimulus, respectively. Then the chronoamperometric response of the working electrode was tested in a miniature well containing 200 μL of PBS (pH 7.4) under the optimized operating electrode potential of −0.35 V. PMA was added into the electrochemical cell at the starting time point (0 s) (b) ESR spectra of $H_2O_2$ released from Hela cells ($5 \times 10^5$ cells per mL) with PMA (10 μg mL$^{-1}$) stimulation for different time periods. (c) ESR spectra of standard $H_2O_2$ solution with known concentrations. It should be noted that 1% (v/v) DMSO (solvent for the PMA) was added into the standard solution to remain consistent with the testing conditions for the real analytical solution. (d) Calibration curve of the intensity of ESR signal *vs* logarithm of the $H_2O_2$ concentration. The inset shows the linear relationship between the amperometric current and the ESR signal intensity. $\Delta i_p$ was defined as the difference between the current intensity at a certain time point and that at the starting time point. $\Delta I_{ESR}$ was defined as the average intensity of the two centered peaks in the ESR spectrum. The data points and error bars represent the mean and the standard deviation, respectively, of at least three independent experiments.

For accurate quantitative determination of the dynamics of extracellular $H_2O_2$ released from the Hela cells, we first read the current intensity at different time points as shown in Fig. 3a. Second, we calculated the corresponding ESR signal intensity according to eqn (I) as shown in the inset of Fig. 3d. Finally, by using the $H_2O_2$ calibration curve obtained by ESR spectroscopy (eqn (II)), we obtained the concentration of the extracellular $H_2O_2$($C_{H_2O_2}$) released from Hela cells after PMA stimulation (Table 1). Thus, with the assistance of the sensitive ESR technique, we avoided the unreliable accuracy of the calibration curve obtained from the single-dimensional electrochemical method, providing a more accurate quantitative detection of $H_2O_2$ in living systems.

As shown in Table 1, with a known electrolyte volume ($V$) of 200 μL and the Avogadro constant ($N_A$) of $6.02 \times 10^{23}$, the total number of extracellular $H_2O_2$ molecules ($n_{tot(H_2O_2)}$) was calculated to be about $10^{15}$ ($n_{tot(H_2O_2)} = C_{H_2O_2} \times V \times N_A$). In our analytical system, the total number of Hela cells grown on the

**Table 1** Quantification of extracellular $H_2O_2$ at different time points

| Time/min | $\Delta i_p$/μA | $\Delta I_{ESR}$ | $C_{H_2O_2}$/M | $n_{tot(H_2O_2)}$ | $n_{ave(H_2O_2)}$ |
|---|---|---|---|---|---|
| 20 | 0.539 | 459.562 | $2.34 \times 10^{-6}$ | $2.82 \times 10^{14}$ | $2.82 \times 10^{9}$ |
| 25 | 0.712 | 570.563 | $6.04 \times 10^{-6}$ | $7.27 \times 10^{14}$ | $7.27 \times 10^{9}$ |
| 30 | 0.818 | 665.375 | $1.34 \times 10^{-5}$ | $1.62 \times 10^{15}$ | $1.62 \times 10^{10}$ |
| 35 | 0.907 | 718.000 | $2.10 \times 10^{-5}$ | $2.53 \times 10^{15}$ | $2.53 \times 10^{10}$ |
| 40 | 0.977 | 779.875 | $3.53 \times 10^{-5}$ | $4.25 \times 10^{15}$ | $4.25 \times 10^{10}$ |

The data in this table is the average value from three replicate experiments.

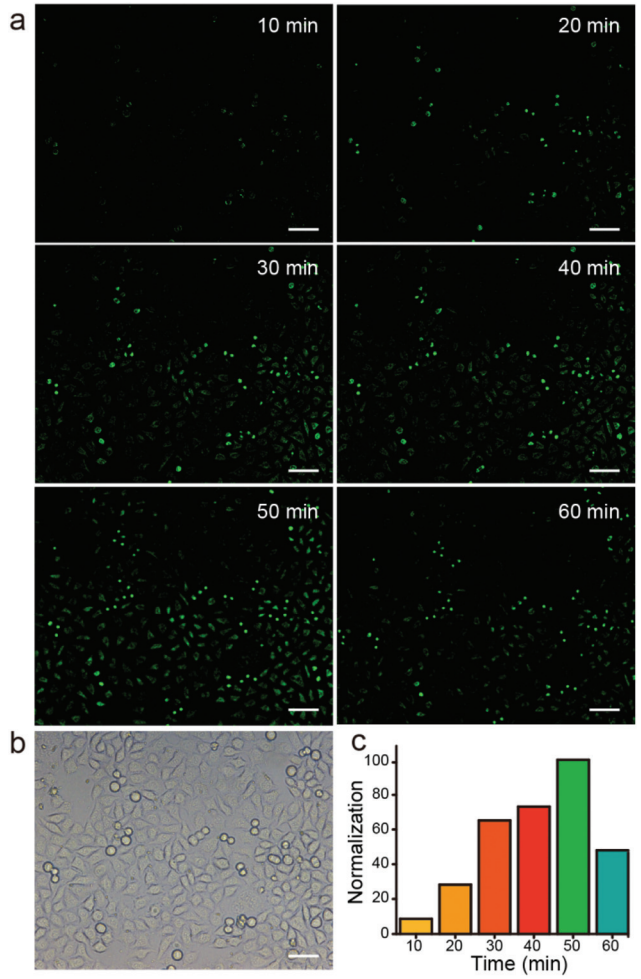


**Fig. 4** (a) Fluorescence images of Hela cells ($5 \times 10^5$ mL$^{-1}$) under PMA (10 μg mL$^{-1}$) stimulation at 10, 20, 30, 40, 50, and 60 min respectively. Excitation wavelength: 488 nm. Scale bars, 25 μm. (b) Bright field image of Hela cells. Scale bar, 25 μm. (c) Normalized fluorescence intensity histogram of the fluorescence images in (a). Relative values normalized to the maximum amount (set to 100) across fluorescence intensity for $H_2O_2$ are shown.

working electrode was $10^5$ *via* multiplying the inoculated concentration of Hela cells ($5 \times 10^5$ cells per mL) by the inoculated volume (200 μL). Therefore, the average number of extracellular $H_2O_2$ molecules released per cell ($n_{ave(H_2O_2)}$) was calculated to be about $10^{10}$, slightly lower than that reported by Li *et al.* ($10^{11}$).[21]

### Simultaneous detection of intracellular and extracellular $H_2O_2$

Although $H_2O_2$ possesses the ability to cross cell membranes,[48] there might be a difference between the concentrations of intracellular and extracellular $H_2O_2$ because some intracellular enzymes such as catalase and other peroxidases can efficiently break down $H_2O_2$, that is, the intracellular $H_2O_2$ concentration depends on its generation rate, as well as its consumption rate.[49] And it is not suitable to only use the extracellular $H_2O_2$ level for comprehensively investigating the related cellular activity. Therefore, simultaneous detection of the dynamics of both intra- and extra-cellular $H_2O_2$ is essential for more comprehensive monitoring of cellular activity.[50] Our prepared working electrode not only displays high electrochemical performance but also possesses good optical transparency, allowing simultaneous detection of extracellular $H_2O_2$ with chronoamperometry and visualization of intracellular $H_2O_2$ by fluorescence microscopy. Prior to experiments, Hela cells were stained with a cell-permeable specific $H_2O_2$ probe BES–$H_2O_2$–AC.[51]

Upon PMA stimulation, the fluorescence intensity in the cytoplasm of Hela cells continued to increase in the range of 0 to 50 min (Fig. 4a), corresponding to the changing trend of the extracellular $H_2O_2$ concentration in the aforementioned result of electrochemical detection. In contrast, no fluorescence could be detected in the control experiment without stimulation, indicating that the constant intracellular $H_2O_2$ production was induced by PMA. When the incubation time becomes longer than 50 min, a decrease in fluorescence intensity was observed. The normalized data displayed that the fluorescence intensities were 9%, 28%, 65%, 73%, 100%, and 48% at 10, 20, 30, 40, 50, and 60 min, respectively (Fig. 4c), suggesting that the intracellular $H_2O_2$ concentration reached the highest level at about 50 min and began to decrease. The decrease of the intracellular $H_2O_2$ concentration in the range of 50 to 60 min could be due to the decrease in cellular $H_2O_2$ production caused by the negative feedback regulation of $H_2O_2$ signaling through intracellular sensor proteins under the condition of a relatively high level of $H_2O_2$,[52] and continuous consumption of $H_2O_2$ in the presence of intracellular scavenger catalase.[4,53] Simultaneous real-time detection of intra- and extra-cellular $H_2O_2$ generation offers an advantage to verify and compare their measured signals, thus avoiding false positive detections and ensuring the accurate evaluation of cellular activities.

## Conclusions

The accurate and comprehensive *in situ* detection of the real-time dynamics of cellular $H_2O_2$ was realized by a combination of electrochemical, ESR, and fluorescence methods. In this multi-dimensional analytical system, a reliable quantitative electrochemical detection of extracellular $H_2O_2$ released from living cells was achieved by the assistance of ESR calibration, avoiding the unreliable accuracy of calibration curves obtained from the single-dimensional electrochemical method. And the transparent property of the graphene-based electrode allows the efficient penetration of excitation and emission light to realize simultaneous high-resolution optical detection of intracellular $H_2O_2$, enabling a more in-depth and comprehensive analysis towards $H_2O_2$ related cellular activities. This will be helpful to thoroughly understand the redox changes associated with cell expansion and malignant transformation. Our multi-dimensional approach can also be extended to other dynamic monitoring platforms, and be applied to analysis of the key

biological processes in living systems, which is potentially useful in cancer diagnosis and progress.

## Acknowledgements

The authors acknowledge the financial support from the National Natural Science Foundation of China (grant no. 21573049, 21422303, 81602643), the National Key R&D Program "nanotechnology" special focus (2016YFA0201600), the Beijing Natural Science Foundation (2142036), the Knowledge Innovation Program and the Youth Innovation Promotion Association of CAS, and the CAS Key Laboratory for Nanosystem and Hierarchical Fabrication.

## References

1 B. D'Autreaux and M. B. Toledano, *Nat. Rev. Mol. Cell Biol.*, 2007, **8**, 813–824.
2 J. L. Martin-Ventura, J. Madrigal-Matute, R. Martinez Pinna, P. Ramos-Mozo, L. M. Blanco-Colio, J. A. Moreno, C. Tarin, E. Burillo, C. E. Fernandez-Garcia and J. Egido, *Thromb. Haemostasis*, 2012, **108**, 435–442.
3 E. A. Veal, A. M. Day and B. A. Morgan, *Mol. Cell.*, 2007, **26**, 1–14.
4 M. Giorgio, M. Trinei, E. Migliaccio and P. G. Pelicci, *Nat. Rev. Mol. Cell Biol.*, 2007, **8**, 722–728.
5 T. Finkel and N. J. Holbrook, *Nature*, 2000, **408**, 239–247.
6 J. E. Klaunig and L. M. Kamendulis, *Toxicol. Sci.*, 1999, **52**, 101–106.
7 K. J. Barnham, C. L. Masters and A. I. Bush, *Nat. Rev. Drug Discovery*, 2004, **3**, 205–214.
8 R. A. Miller and B. E. Britigan, *Clin. Microbiol. Rev.*, 1997, **10**, 1–18.
9 D. R. Gough and T. G. Cotter, *Cell Death Dis.*, 2011, **2**, e213.
10 D. Srikun, E. W. Miller, D. W. Domaille and C. Chang, *J. Am. Chem. Soc.*, 2008, **130**, 4596–4597.
11 S. G. Rhee, *Science*, 2006, **312**, 1882–1883.
12 C. Li, H. Zhang, P. Wu, Z. Gong, G. Xu and C. Cai, *Analyst*, 2011, **136**, 1116–1123.
13 G. Bartosz, *Clin. Chim. Acta*, 2006, **368**, 53–76.
14 T. Matoba, H. Shimokawa, K. Morikawa, H. Kubota, I. Kunihiro, L. Urakami-Harasawa, Y. Mukai, Y. Hirakawa, T. Akaike and A. Takeshita, *Arterioscler. Thromb. Vasc.*, 2003, **23**, 1224–1230.
15 B. C. Dickinson, C. Huynh and C. J. Chang, *J. Am. Chem. Soc.*, 2010, **132**, 5906–5915.
16 Y. Hitomi, T. Takeyasu, T. Funabiki and M. Kodera, *Anal. Chem.*, 2011, **83**, 9213–9216.
17 B. Wang, B. Li, Z. Wang, G. Xu, Q. Wang and S. Dong, *Anal. Chem.*, 1999, **71**, 1935–1939.
18 W. Huang, J. Jia, Z. Zhang, X. Han, J. Tang, J. Wang, S. Dong and E. Wang, *Biosens. Bioelectron.*, 2003, **18**, 1225–1230.
19 J. Tang, B. Wang, Z. Wu, X. Han, S. Dong and E. Wang, *Biosens. Bioelectron.*, 2003, **18**, 867–872.
20 S. Guo, D. Wen, Y. Zhai, S. Dong and E. Wang, *ACS Nano*, 2010, **4**, 3959–3968.
21 C. X. Guo, X. T. Zhefng, Z. S. Lu, X. W. Lou and C. M. Li, *Adv. Mater.*, 2010, **22**, 5164–5167.
22 J. Wang, L. Li, W. Huang and J. Cheng, *Anal. Chem.*, 2010, **82**, 5380–5383.
23 G. Xu and S. Dong, *Electroanalysis*, 1999, **11**, 1180–1184.
24 H. Fang, Y. Pan, W. Shan, M. Guo, Z. Nie, Y. Huang and S. Yao, *Anal. Methods*, 2014, **6**, 6073–6081.
25 Y. Zhang, C. Wu, X. Zhou, X. Wu, Y. Yang, H. Wu, S. Guo and J. Zhang, *Nanoscale*, 2013, **5**, 1816–1819.
26 H. Sies, *Protein sensors and reactive oxygen species: selenoproteins and thioredoxin*, Academic Press, 2002.
27 J. J. Zhang, F. F. Cheng, T. T. Zheng and J. J. Zhu, *Anal. Chem.*, 2010, **82**, 3547–3555.
28 H. Guo, H. Aleyasin, B. C. Dickinson, R. E. Haskew-Layton and R. R. Ratan, *Cell Biosci.*, 2014, **4**, 64.
29 Y. Liu, D. Yu, C. Zeng, Z. Miao and L. Dai, *Langmuir*, 2010, **26**, 6158–6160.
30 Y. Du, S. Guo, S. Dong and E. Wang, *Biomaterials*, 2011, **32**, 8584–8592.
31 L. Fan, Q. Zhang, K. Wang, F. Li and L. Niu, *J. Mater. Chem.*, 2012, **22**, 6165–6170.
32 A. K. Kafi, G. Wu and A. Chen, *Biosens. Bioelectron.*, 2008, **24**, 566–571.
33 W. Chen, S. Cai, Q. Q. Ren, W. Wen and Y. D. Zhao, *Analyst*, 2012, **137**, 49–58.
34 P. Furbert, C. Lu, N. Winograd and L. DeLouise, *Langmuir*, 2008, **24**, 2908–2915.
35 X. Zhong, G. S. Qian, J. J. Xu and H. Y. Chen, *J. Phys. Chem. C*, 2010, **114**, 19503–19508.
36 Y. Shao, J. Wang, H. Wu, J. Liu, I. A. Aksay and Y. Lin, *Electroanalysis*, 2010, **22**, 1027–1036.
37 J. Li, S. Guo, Y. Zhai and E. Wang, *Electrochem. Commun.*, 2009, **11**, 1085–1088.
38 D. A. Brownson, D. K. Kampouris and C. E. Banks, *Chem. Soc. Rev.*, 2012, **41**, 6944–6976.
39 Y. Yao, Y. Ding, L. S. Ye and X. H. Xia, *Carbon*, 2006, **44**, 61–66.
40 K. Fang, Y. Yang, L. Fu, H. Zheng, J. Yuan and L. Niu, *Sens. Actuators, B*, 2014, **191**, 401–407.
41 H. Asakawa, K. Mochitate and T. Haruyama, *Anal. Chem.*, 2008, **80**, 1505–1511.
42 F. Lazaro-Dieguez and G. Egea, *Mod. Res. Educ. Top. Microsc.*, 2014, 362–369.
43 L. Y. Chen, Y. H. Tang, K. Wang, C. B. Liu and S. L. Luo, *Electrochem. Commun.*, 2011, **13**, 133–137.
44 X. Wang, A. Sumboja, M. Lin, J. Yan and P. S. Lee, *Nanoscale*, 2012, **4**, 7266–7272.
45 Q. Y. Lin, L. J. Jin, Z. H. Cao, Y. N. Lu, H. Y. Xue and Y. P. Xu, *Phytother. Res.*, 2008, **22**, 740–745.
46 E. M. Ceresa, L. Burlamacchi and M. Visca, *J. Mater. Sci.*, 1983, **18**, 289–294.
47 R. Weinstain, E. N. Savariar, C. N. Felsen and R. Y. Tsien, *J. Am. Chem. Soc.*, 2014, **136**, 874–877.

 

48 G. J. DeYulia, J. M. Cárcamo, O. Bórquez-Ojeda, C. C. Shelton and D. W. Golde, *Proc. Natl. Acad. Sci. U. S. A.*, 2005, **102**, 5044–5049.
49 X. Liu and J. L. Zweier, *Free Radical Biol. Med.*, 2001, **31**, 894–901.
50 S. Andreescu and M. Hepel, *Oxidative Stress: Diagnostics, Prevention, and Therapy*, American Chemical Society, 2011.
51 H. Maeda, Y. Fukuyasu, S. Yoshida, M. Fukuda, K. Saeki, H. Matsuno, Y. Yamauchi, K. Yoshida, K. Hirata and K. Miyamoto, *Angew. Chem., Int. Ed.*, 2004, **43**, 2389–2391.
52 E. A. Veal, A. M. Day and B. A. Morgan, *Mol. Cell*, 2007, **26**, 1–14.
53 J. M. Li, H. Zhou, Q. Cai and G. X. Xiao, *Gastroenterol.*, 2003, **9**, 562–567.